

Influence of Spray Angle on the Pore and Crack Microstructure of Plasma-Sprayed Deposits

Jan Ilavsky,[†] Andrew J. Allen,['] Gabrielle G. Long,['] and Susan Krueger

National Institute of Standards and Technology, Gaithersburg, Maryland 20899

Christopher C. Berndt['] and Herbert Herman^{*}

State University of New York at Stony Brook, Stony Brook, New York 11794

To understand the influence of processing parameters on the microstructure of plasma-sprayed deposits, small-angle neutron scattering measurements were made of the processing-parameter-dependent specific surface area of the voids in gray alumina deposits. These studies indicate that the voids are in the form of pores between the splats and around inclusions or unmelted particles, and are also in the form of cracks within the splats which may develop during cooling. The porous volume increases as the angle between the spray gun and the substrate (the "spray angle") decreases. This study also indicates that the cracks are preferentially oriented, and that the crack orientation also depends on the spray angle. The interlamellar pores, however, are preferentially oriented parallel to the substrate surface, and the orientation of the pore is independent of the spray angle.

I. Introduction

POROSITY, a common feature of the microstructure of plasma-sprayed deposits, is such an important factor in determining the physical properties of these materials that the deposits are usually characterized by the volume of the voids and the specific surface areas of the voids.¹ There are numerous techniques to measure porosity, but these often yield model-dependent results² that are a function of the assumptions underlying the data analysis. In this regard, there is a distinct advantage in using small-angle neutron scattering in that the specific surface areas of both the open and the closed porosity are directly and model-independently related to the amount of scattering.

Plasma-sprayed deposits are composed of splats created by the rapid solidification of molten or semimolten feedstock particles either on a substrate or on a layer of previously solidified particles.³ Rapid cooling of the particles results in the formation of metastable phases and complex microstructures. The main features in the microstructure of plasma-sprayed coatings, shown in Fig. 1, are the splats, separated by interlamellar pores, voids around unmelted particles, and cracks that are most likely formed upon cooling.⁴⁻⁶

The plasma-spray process is specified by the associated processing parameters, where these influence the properties of the resultant deposits.^{7,8} Changing the processing parameters is the most common way of varying the (mechanical, thermal, electrical, ...) properties of the deposits. What is required is a

systematic investigation of processing-microstructure relationships so that process models can ultimately be developed which offer quantitative predictability of product microstructures.

One parameter which is thought to have a significant influence on the microstructure, and hence on the properties of plasma-sprayed deposits, is the spray angle.^{9,10} The spray angle is defined as the angle between the axis of the spray torch and the surface of the substrate; see the upper panel of Fig. 2. This angle is usually close to 90°, but it will vary, for example, if the substrate has a nonplanar surface, or if there is a broad distribution of impact speeds and spray angles" in the plasma cone.

The thickness profile (i.e., the "footprint") of the deposit is expected to change as a function of the spray angle. The predicted thickness profiles, shown in Fig. 3, were calculated from the measured footprint of the present plasma-spray system for a 90° spray angle using a Gaussian distribution to describe the distribution of particulates in the plasma cone. A variation in the particle impact angle results in a change in the average splat shape^{12,13} as well as changes in other characteristics of the spray process, e.g., the component of the impact velocity perpendicular to the substrate. The research which forms the subject of this paper was aimed at measuring the changes in the plasma-sprayed deposit pore and crack microstructure as a function of spray angle in an effort to gain a quantitative understanding of the influence of the spray angle in practical applications.

II. Experimental Techniques

(I) Sample Fabrication

The samples were prepared using a water-stabilized PAL 160[†] plasma torch (from the Institute of Plasma Physics, Czech Academy of Science in the Czech Republic) at the Thermal Spray Laboratory of the State University of New York at Stony Brook. This high-throughput system operates using an electrical input of about 160 kW (320 V and 500 A dc). To make use of the high input power, water is the plasma medium rather than the more-commonly-used gases such as hydrogen, nitrogen, argon, or helium. This system can be used to fabricate deposits with characteristics similar to those of materials prepared by means of conventional atmospheric plasma-spray systems.¹⁴ The deposition time, however, is shortened significantly because of the 10-fold increase in the throughput of this system. For the purpose of rastering, the entire plasma-spray system was mounted on a GMF Fanuc six-axis articulated robot (Model S400).

The feedstock material was (Norton 101) gray alumina composed of α -phase alumina (α -Al₂O₃) and 3 wt% titania (TiO₂). The particle sizes ranged between approximately 35 and

R. W Rice—contributing editor

Manuscript No. 192226. Received October 31, 1995; approved September 9, 1996.

[†]Member, American Ceramic Society.

[']Current address: Institute of Plasma Physics, Academy of Sciences CR, P.O. Box 17, 182 00 Praha 8, Czech Republic.

^{*}Information on commercial products is given for completeness and does not necessarily constitute or imply their endorsement by the National Institute of Standards and Technology.

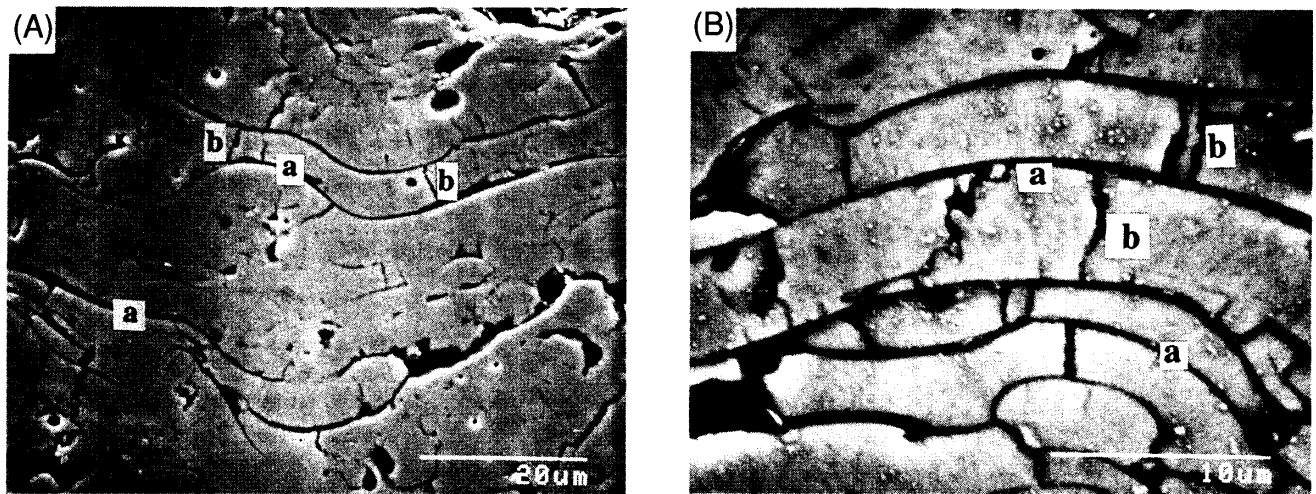


Fig. 1. Typical microstructure of plasma-sprayed ceramic deposits. These are micrographs of the cross sections of an yttria-stabilized-zirconia deposit, which offers a clearer picture of the plasma-sprayed microstructure than plasma-sprayed gray alumina. Two basic types of voids are seen: (a) interlamellar voids and (b) cracks. Gray alumina deposits contain very similar microstructures.

150 μm . After spraying, the gray alumina deposits were composed of a mixture of metastable phases, mostly γ -phase and 6-phase alumina, with a minority component of α -phase alumina. The density of γ -phase and 6-phase alumina is about $3.6 \text{ g}\cdot\text{cm}^{-3}$, while the density of α -phase alumina is about $4.0 \text{ g}\cdot\text{cm}^{-3}$.¹⁵

The substrate coupons were made of mild steel, 2.5 cm long by 2.5 cm wide by 0.25 cm thick. They were prepared by sand blasting and were covered with a thin layer of aluminum. Free-standing samples of plasma-sprayed gray alumina were obtained by dissolving the aluminum layer in 20% HCl.

The sample axes, which are attached to the substrate, are defined in the upper panel of Fig. 2. The plasma-spray system was rastered in the YZ plane, as shown in the lower panel of Fig. 2. Before spraying, the substrates were preheated by one

cycle (four passes) of the plasma-spray system in the same pattern used for deposition, but without powder flow.

The torch then passed over the substrates four times with the spray system moving across in Y and down in Z. After the substrates were covered by means of these four passes, the spray system was returned to its position above the samples and the cycle was repeated until a deposit of the required thickness was achieved. This required 20 to 30 cycles. The final deposit thicknesses were 5 to 6.5 mm, and thus deposits were formed at the rate of 0.2 to 0.25 mm per cycle. The spray angles were 90° , 70° , 50° , and 30° , measured from the substrate surface to the axis of the plasma spray torch in the XY plane. The spray distance (300 mm) was measured along the axis of the spray system between the nozzle of the spray gun and the surface of the substrate.

(2) Analytical Techniques

The main technique for studying the porous microstructures of plasma-sprayed deposits was small-angle neutron scattering (SANS), carried out on the 8 m SANS instrument at the NIST Cold Neutron Research Facility at the National Institute of Standards and Technology in Gaithersburg, MD. The same materials were studied by means of X-ray diffraction (XRD) to determine the phases present, and by means of mercury-intrusion porosimetry (MIP) and Archimedeian (water displacement) porosimetry to determine the porosity.

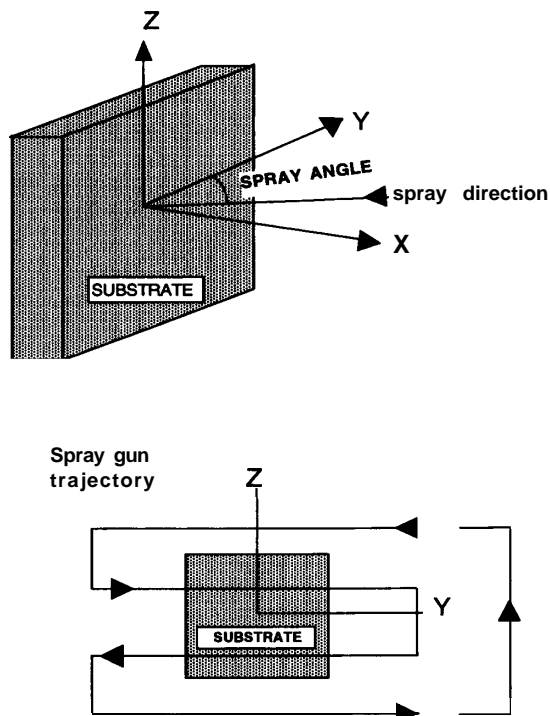


Fig. 2. Definition of the spray angle and sample axes (upper panel) and schematic of the spray apparatus trajectory (lower panel).

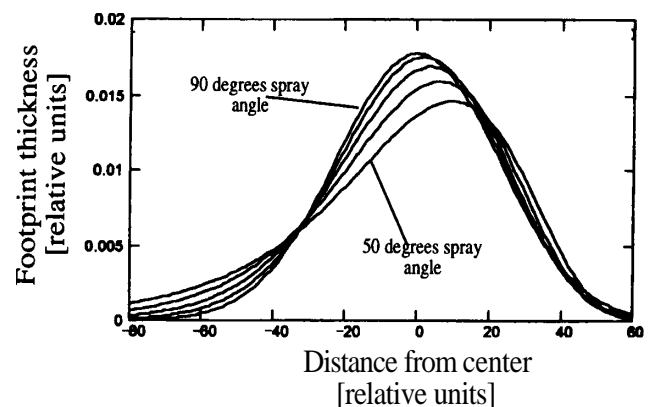


Fig. 3. Thickness profile ("footprint") of the plasma-spray deposit as a function of the spray angle. The three intermediate curves between 90° and 50° are 80° , 70° and 60° spray angles, respectively.

(A) **X-ray Diffraction:** XRD was used to determine the phase composition of the plasma-sprayed materials. From the phase determinations, the skeletal density of void-free material was determined. A standard Phillips diffractometer, equipped with a Cu anode X-ray tube, was used. Integrated intensities were derived by fitting Lorentzian line shapes to the measured data. The reference intensity ratio method¹⁶⁻²⁰ was used in the phase analysis. This method relates the phase content to the ratios of the integrated intensities of selected peaks arising from a particular phase to the total integrated intensity of peaks arising from all of the phases in the material. Intensities of the (104) and (113) peaks from the α -phase, the (400) peak from the γ -phase, and the (400) and (004) peaks from the δ -phase were used in the analysis.²¹ The peaks arising from the metastable γ -phase and from the δ -phase could not be separated, so they were combined into a single nominal phase for the analysis. The phase weight content was calculated from Eq. (1):

$$w_i = \frac{D_i I_i}{D_\alpha I_\alpha + D_\gamma I_\gamma + I_\delta} \quad (1)$$

where i represents one of the phases, D_i is the experimentally established coefficient for the i th phase, and I_i is the intensity (or the sum of the intensities) of the peak (or peaks) of the i th phase, as discussed above. The data were calibrated using measurements from samples of known phase content which were prepared by mixing known quantities of as-received feedstock (α -phase alumina) into pulverized plasma-spray deposit material (which was mainly γ -phase and δ -phase alumina).

(B) **Mercury Intrusion Porosimetry:** MIP is based on the intrusion of mercury into the pores of a sample as a function of pressure. The radius, r , of a void that is filled at a given pressure is given by Washburn's equation:

$$P_h = -(2\gamma/r) \cos \theta \quad (2)$$

where P_h is the mercury pressure, γ is the surface tension of mercury ($480 \times 10^{-3} \text{ N}\cdot\text{m}^{-1}$ [erg cm^{-2}]) and θ is the wetting or contact angle (which for most materials is close to 140° (Ref. 22)). Void diameters from about 100 μm , at pressures below atmospheric pressure, to about 20 \AA , at pressures of approximately 22.8 MPa, can be measured.²³

The MIP data analysis assumes rod-shaped voids connected to the surface by voids of the same or greater diameter. Voids connected to the surface via smaller-diameter voids (e.g., bottle-neck pores) are assigned the volume of a void with the diameter of these necks. Thus, MIP determinations of void sizes are typically shifted to smaller diameters.

(C) **Archimedean Porosimetry:** In the Archimedean method, the sample weight is determined under three conditions: dry, after filling the pores with water, and with the sample buoyed by Archimedes forces (i.e., the weight in water). The method used in this study was a modified version of the standard method,²⁴ in that the samples were soaked under low vacuum overnight rather than boiled in water for 2 h, which is the usual practice. The overnight soaking was intended to limit the interaction between the metastable alumina phases and the water.

Both the MIP and the Archimedean methods enable the derivation of the as-received and the residual density of the samples, i.e., the open porosity and the residual density. Comparing the residual density with the skeletal density from X-ray diffraction analysis (and the known density of alumina phases), the amount of closed porosity can be established.

(D) **Small-Angle Neutron Scattering:** SANS was recently applied to processing-microstructure studies of the sintering of alumina²¹ and other ceramic materials.²⁶ In that research, the sizes of the pores were determined by means of multiple small-angle neutron scattering, and their total specific surface area was derived from the terminal slope in SANS spectra, i.e., Porod scattering.²⁷ Porod scattering measurements are particularly useful in that they enable a direct determination of the surface areas of both the open and the closed voids in a material,

independent of the void morphology. The results derived from Porod scattering by plasma-sprayed gray alumina, as a function of spray angle, are the main subject of this paper.

A schematic of the SANS experiment is shown in Fig. 4. A beam of cold neutrons, with wavelength $\lambda = 6 \text{ \AA}$ selected by the velocity selector, passes through several collimating apertures before passing through the plasma-deposited sample. These neutrons are scattered within the sample and are measured on the two-dimensional detector.

The voids and the grains within the free-standing plasma-sprayed samples have different scattering length density, ρ , causing some of the neutrons to be scattered at the void/grain interfaces. The scattered intensity, I , is a function of the scattering wave vector Q , where $|Q| = (4\pi/\lambda) \sin \theta$, and 2θ is the scattering angle.²⁸ $I(Q)$ depends on the amount, ϕ , of porosity, on the scattering contrast (which is the square of the difference in scattering length densities between the grains and the voids, $(\Delta\rho)^2$), and on the distribution of void sizes. When the microstructure of a scattering sample is isotropic, the scattered intensity depends simply on $Q = |Q|$, rather than on Q .

If only a small fraction of the incident neutrons are small-angle scattered, and the scattering features are in the size regime from 0.2 nm to 1 μm , then a SANS analysis assuming single-scattering and diffraction theory is used. For anisotropic microstructures, the scattered profile as a function of Q can be used to gain information on the shape, size distribution, volume fraction, and surface areas of the scattering features, provided that the scattered intensity is averaged over all orientations of Q . For a particular Q , the information refers to dimensions parallel to Q .^{27,28} For copious numbers of scattering voids in the 0.1 to 10 μm size range, as is observed in plasma-sprayed ceramics, a multiple-scattering formulation (MSANS) must be employed.²⁹ It is still possible to extract information on the size, porosity, pore shape, and anisotropy in the MSANS case, and achieving this is the subject of ongoing work by the authors. In this paper, however, we limit the discussion to an analysis of the data in the single-scattering Porod regime, which occurs at large Q even when multiple scattering^{30,31} is present at low Q .

The Porod scattering regime^{27,28,32} extends over the region in the data for which $QL > 3$, where L is the smallest dimension in the scatterers. For isotropically distributed microstructures, the scattering cross section $d\Sigma/d\Omega$ (or the scattered intensity) is given by the Porod scattering relationship:

$$\frac{d\Sigma(Q)}{d\Omega} = \frac{2\pi(\Delta\rho)^2 S_v}{Q^4} \quad (3)$$

where S_v is the total specific surface scattering area of the voids. Since the material is a two-phase (grains + voids) system, where the scattering occurs at the boundaries between solid and void, S_v is the total pore/solid and crack/solid surface area per unit sample volume. To obtain a complete description of the void system, the values for S_v need to be used together with information on the sizes, volumes, and shapes of the voids. Such a description is beyond the scope of this paper.

Electron microscopy results³³ have shown that the voids in plasma-sprayed ceramics are polydisperse in both size and shape. Furthermore, the voids are preferentially oriented when viewed in the YX or the ZX planes. Only the microstructure viewed in the YZ plane, when the coating was formed at a 90° spray angle, is isotropic. The presence of one circularly symmetric direction (the plane perpendicular to the X direction) in the plasma-sprayed microstructure will be key in enabling a quantitative three-dimensional analysis of the microstructure from the scattering data.

To derive the total surface area of voids within an anisotropic material, the scattered intensity can be measured and averaged for all sample-beam orientations, covering all possible angles. For plasma-sprayed samples, this procedure would not necessarily distinguish among the distinct structures in the deposit. Instead, we devised a method for analyzing the scattering along selected directions of Q , enabling us to derive separately the

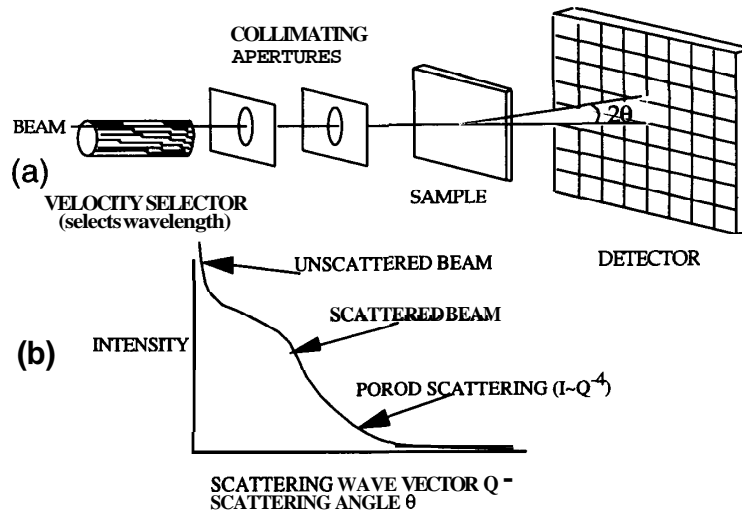


Fig. 4. Schematic of (a) the SANS apparatus and (b) a scattering curve.

parameters of the individual void structures which contribute to the anisotropic scattering patterns.

As indicated above, the microstructure of plasma-sprayed deposits is anisotropic in each of two orthogonal planes, but is circularly symmetric in the third. For monodispersed spheroids (ellipsoids of revolution) with orthogonal radii R , R , and βR , the anisotropic Porod scattering can be calculated analytically. Following the analysis of Hamzeh and Bragg³⁴ Eq. (3) becomes

$$\frac{d\Sigma(\vec{Q})}{d\Omega} = \frac{2\pi|\Delta\rho|^2 3\phi}{Q^4} \frac{\beta}{R [1 + (\beta^2 - 1)X^2]^2} \quad (4)$$

where ϕ is the volume fraction of the spheroidal voids and $X = \cos \eta$, where η is the angle between Q and the βR axis of spheroidal symmetry. ($X = 0$ when Q is perpendicular to the βR axis and $X = 1$ when Q is parallel to the βR axis.) Note that for spheres (i.e., $\beta = 1$) Eq. (4) reduces to Eq. (3) since $S_v = 3\phi/R$.

The anisotropy in the Porod scattering, given by Eq. (4), is strongly amplified with the shape of the scatterers. While the anisotropy in the scattering is not strictly spheroidal itself, even mildly oblate spheroidal scatterers, of fixed orientation, will give markedly prolate anisotropic Porod scattering. Similarly, mildly prolate scatterers, of fixed orientation, will give markedly oblate Porod scattering.

In practice, the anisotropy in the Porod scattering depends not only on the individual pore shapes and preferred alignments, but also on the polydispersity of pore shapes and sizes, and to some extent on the surface roughness. High surface roughness, and considerable polydispersity in pore shapes and sizes, would give anisotropic Porod scattering that is linearly proportional to the interfacial surface area projection in the plane perpendicular to Q .^{27,28} Even for monodisperse spheroids, Eq. (4) must be averaged over the orientational distribution. For random orientations, the anisotropy disappears and Eq. (3) is recovered. However, in the present case of two coexisting pore/crack morphologies with different preferred orientations and sizes and with relatively smooth interfacial surfaces and geometric symmetries (e.g., oblate spheroidal cracks with parallel sides), Eq. (4) is illustrative of the coexisting strong anisotropies that may be observable in the Porod scattering by plasma-sprayed deposits.

It should be noted that particular preferred orientational distributions of the scatterers may be masked in the anisotropy of the Porod scattering. For example, a two-dimensional random orientational distribution of oblate scatterers, all with a short βR axis approximately in one plane, would give rise to Porod scattering that is also oblate in its anisotropy, with the axis of symmetry and the direction of least Porod scattering perpendicular to the orientational averaging plane.

If the Porod scattering can be measured for all orientations of Q over 4π solid angle, none of the above uncertainties in pore shape or morphology prevents a determination of the total interfacial surface area per unit sample volume, $S_{v\text{TOTAL}}$. By averaging $d\Sigma(Q)/d\Omega$ over all orientations of Q , we obtain

$$\left\langle \frac{d\Sigma}{d\Omega} \right\rangle_{\text{ORIENTATION}} = \frac{2\pi|\Delta\rho|^2 S_{v\text{TOTAL}}}{Q^4} \quad (5)$$

where $\langle \dots \rangle$ implies an orientational average. Equation (5) reduces to Eq. (3) in the case of random orientations or an isotropic microstructure. It is important to note that when different coexisting pore morphologies can be discerned from the orientational variation of $d\Sigma(Q)/d\Omega$, these anisotropic components can be orientationally averaged separately. Thus, $S_{v\text{TOTAL}(i)}$ can be determined for the i th pore/crack morphology in the system.

III. Results

(1) X-ray Diffraction

Analysis of the X-ray diffraction data indicated that the proportion of $\alpha\text{-Al}_2\text{O}_3$ varied with the spray angle. This suggested that there were changes in the solidification process and changes in the rate of feedstock melting as a function of spray angle. The minimum α -phase content was found for a spray angle of 50° . These results, together with the skeletal densities (i.e., the densities of 100% dense, void-free material comprised of α -, γ -, and δ -phases in the measured composition) are shown in Table I.

(2) Mercury Intrusion and Archimedes Porosimetry

Table II displays the results derived from the intrusion techniques and Figs. 5 and 6 display the Archimedes and MIP results graphically. The MIP results include the open porosity (i.e., the volume available for intrusion), the residual density (which enables a determination of the volume of closed porosity), and information on pore size. The open porosity and the density measurements require no assumptions concerning the

Table I. X-ray Diffraction Results

Spray angle (deg)	Weight fraction of α -alumina (%)	Skeletal density* ($\times 10^3 \text{ kg}\cdot\text{m}^{-3}$)
90	24	3.70
70	15	3.66
50	3	3.61
30	20	3.68

*The standard uncertainty is 5%. The standard uncertainty is $0.02 \times 10^3 \text{ kg}\cdot\text{m}^{-3}$.

Table II. Water Immersion and Mercury Intrusion Porosimetry Results

Spray angle (deg)	MIP open porosity [†] (%)	MIP closed porosity* (%)	MIP total porosity* (%)	Archimedes open porosity [†] (%)	Archimedes closed porosity* (%)	Archimedes total porosity [‡] (%)	MIP residual density [†] ($\times 10^3 \text{ kg}\cdot\text{m}^{-3}$)	Archimedes residual density [‡] ($\times 10^3 \text{ kg}\cdot\text{m}^{-3}$)	MIP mean pore size (μm)
90	4.8	3.9	8.7	3.7	3.9	7.6	3.49	3.49	0.18
70	6.7	4.4	11.1	5.3	7.4	12.7	3.50	3.39	0.48
50	7.5	3.0	10.5	7.2	3.6	10.8	3.50	3.48	0.54
30	8.7	13.9	22.6	14.3	8.4	22.7	3.17	3.37	0.76

[†]The standard uncertainty is 0.5%. ^{*}The standard uncertainty is 1.5%. [‡]The standard uncertainty is 2.0%. [§]The standard uncertainty is $0.02 \times 10^3 \text{ kg}\cdot\text{m}^{-3}$.

pore shape, while the derivation of pore sizes involves assuming a cylindrical pore shape.

The porosimetry results indicate that the porosities (total and open) increase with decreasing spray angle, with the porosity in the 30° spray angle sample being more than double that in the 90° spray angle sample. The open porosity increases in the same manner (i.e., as the spray angle decreases), with the largest amount of porosity found for the 30° sample.

In the case of the 30°-spray-angle sample, a significant and reproducible difference between the MIP and the Archimedes determinations of the open porosity was found. This difference suggests that different fractions of the pores are filled during the two types of measurements, perhaps due to the directionality of the MIP experiment. However, the two methods yielded the same result for the total porosity.

(3) Small-Angle Neutron Scattering

In this study, the variation of the Porod constant, $P = Q^4(d\Sigma/d\Omega)$, was followed for different orientations of Q by means of the scattered neutron intensity measured on a two-dimensional detector. For the 90° spray angle sample, for which the neutron beam was incident along the X axis (and spray direction), the circularly symmetric two-dimensional SANS data taken by the area detector could be radially averaged about the incident beam. Application of Eq. (3) to this radially averaged $I(Q)$ data could be used to obtain a single Porod constant, independent of the direction of Q. The scattered intensities in the anisotropic SANS were sector-averaged in 30°-wide angular sectors spaced 15° apart. The sector-averaged $I(Q)$ vs Q data were used to extract an apparent Porod constant for each of the sectors using Eq. (3). These apparent Porod constants were then related back to the Q's given by the orientations of the axes of the sectors. From the apparent Porod constants, apparent surface areas $S_v(Q)$ were derived, also using Eq. (3).

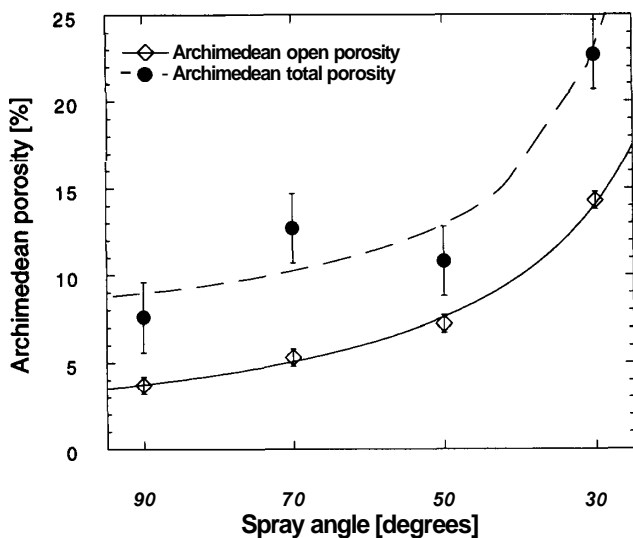


Fig. 5. Archimedes porosity results. The open porosity is derived directly from the Archimedes data; the total porosity is calculated from the density results and from the skeletal density derived from the XRD measurements.

In Table III, and Figs. 7–10, we present the apparent surface areas, $S_v(Q)$, calculated from Eq. (3) for particular orientations of Q. Although the true surface area projections perpendicular to Q are uncertain—being between the values predicted by Eqs. (3) and (4)—the total surface area can be derived by appropriate geometric averaging over 4π steradian of the apparent $S_v(Q)$ data on the YZ, ZX, and XY planes, as indicated in Eq. (5). Furthermore, if the anisotropic data from the XY and ZX planes can be resolved into separate anisotropic components, the circularly symmetric data in the YZ plane can then also be divided into the relative contributions of the microstructural components. Then, the total specific surface areas can be calculated separately for each of the microstructural subsystems. The method for doing this is given below.

Results from the SANS data from the 90° sample are shown in Fig. 7. In Fig. 7(A), the apparent surface area distribution, measured with Q lying in the ZX plane, is shown as a function of the angle between Q and the X axis on a Cartesian plot. It is important to note that the circularly symmetric data in the YZ plane are also seen in the sectors that are 90° from the X axis in the ZX and XY planes. It was found that the data 90° to X correspond, within experimental error, to the result from the YZ plane. This confirms that the analysis procedure is self-consistent, and that an appropriate angular width has been selected for the sector averaging.

A more illuminating way of looking at the data is shown in Fig. 7(B), in which the results shown in Fig. 7(A) are replotted in polar coordinates. The results for $S_v(Q)$ form a bulging ellipse (solid line) which has a primary maximum at 90° and a secondary maximum at 0°. The bulging ellipse can be decomposed into two simple ellipses (dashed lines) using least-squares fitting of ellipsoids to the apparent surface area. The presence of two ellipses is evidence for the presence of two populations of voids in the microstructure. The complementary

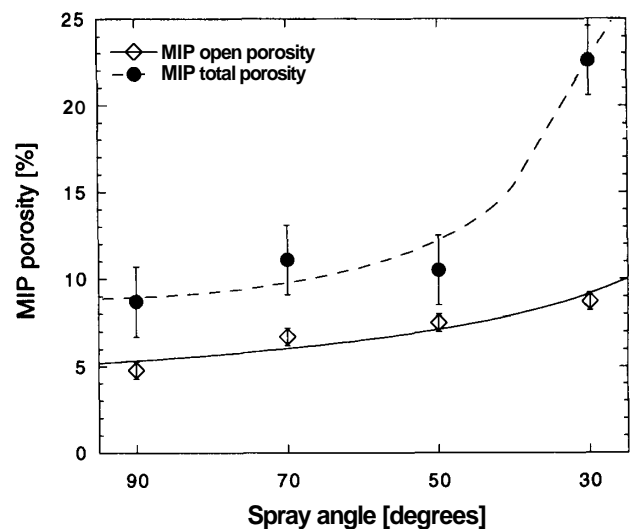


Fig. 6. Mercury intrusion porosimetry results. The open porosity is derived directly from the data; the total porosity is calculated from the density results and from the skeletal density derived from the XRD measurements.

Table III. SANS Results^t

Sample spray angle (deg)	Total specific surface area ($\times 10^6 \text{ m}^2/\text{m}^3$)	Total specific surface area (m^2/kg)	Surface area in the crack system ($\times 10^6 \text{ m}^2/\text{m}^3$)	Surface area in the crack system (m^2/kg)	Surface area in the pore system ($\times 10^6 \text{ m}^2/\text{m}^3$)	Surface area in the pore system (m^2/kg)
90	1.8	530	1.6	470	0.2	60
70	1.6	500	1.5	460	0.1	40
50	1.8	560	1.7	530	0.1	30
30	1.5	530	1.3	460	0.2	70

^tThe total specific surface areas (per unit volume and per unit weight) in the crack and the pore systems were calculated from the Z projections of the data. (The estimated standard uncertainty of the measurements is $0.1 \times 10^6 \text{ m}^2/\text{m}^3$ and $30 \text{ m}^2/\text{kg}$.)

view in the XY plane is shown in Fig. 7(C), where another bulging ellipse is seen, which can likewise be decomposed into two ellipses. A three-dimensional plot is shown in Fig. 7(D). To obtain the total specific surface areas from these results, it is necessary to integrate about the symmetry axis (X) over 4π steradian. Results of the integration are given numerically in Table III and are shown graphically in Figs. 7(B) and (C) as the dot-dash circle.

Proceeding now to data from samples with other spray angles, results for the 70° spray angle sample are shown in Figs. 8(A–C). In this case, the view from the side in the ZX plane (Fig. 8(A)) shows two ellipses which are centered on X and Z. The view from above in the XY plane (Fig. 8(B)), however, shows one ellipse centered on X and another tilted from Y by about 15°. The data from the 50° spray angle sample (Fig. 9) and from the 30° spray angle sample (Fig. 10) are also tilted (by about 15° and 30°, respectively) when viewed from above in the XY plane. Note that since the experimental size of the sector angle was 15°, and the angular width of a sector was 30°, these tilt angles are close to the limits of the experimental resolution.

For all four spray angles, the maximum apparent surface areas in the ZX plane (viewed along Y) were measured for Q oriented 90° to the X axis. This maximum can be associated with voids orientated so that their maximum surface areas in this projection are perpendicular to the deposit surface and parallel to the X axis. For the 90°-spray-angle sample, these voids are the same as those measured when the neutron beam is parallel to the X axis. These voids can be associated with voids or cracks with their long dimension, in this projection, perpendicular to the substrate. A second, smaller, maximum in the surface area was measured for Q oriented 0° to the X axis. This indicates the presence of a second population of voids, with surfaces mostly parallel to the deposit surface. We associate this second population of voids to oblate pores between the splat layers. For the 30° spray angle, however, the alignment is difficult to observe because of the complicated void arrangement.

In the XY plane, viewing along Z, only the sample sprayed at 90° shows the maximum Porod scattering for Q along the Y direction. For other spray angles, the large Porod scattering ellipsoid tilts toward the spray direction. This change in the orientation of the larger oblate ellipsoid shows that, in this projection, the main orientation of the voids (which are associated with the cracks) depends on the spray angle. The smaller Porod scattering prolate ellipsoid (which is associated with the interlamellar pores) remains aligned with its major axis perpendicular to the substrate for all spray angles. The larger Porod scattering ellipsoid lags behind the tilt in the spray direction. For the 50° spray angle sample, for example, this axis turned only about 20°, or about half the tilt in the spray direction.

These effects suggest that the voids associated with intralamellar cracks are influenced by the spray angle, whereas the voids associated with interlamellar pores are not. Despite the very disordered nature of both void morphologies, it is remarkable that they exhibit distinctly different statistical orientational dependencies on the spray angle. It should be noted that, because of the generally disordered nature of the void systems, these effects can only be measured quantitatively by a technique

such as SANS, which yields results that are statistically representative of the undisturbed microstructures.

Thus, we have characterized separately, by means of SANS, the surface area of the cracks and the surface area of the interlamellar pores. Finally, Table III indicates that the total specific surface area of one system (related to the intralamellar cracks) contains most (more than 85%) of the total surface area within the sample, while the other system (related to the interlamellar pores) contains only 5–15% of the total surface area.

IV. Discussion and Conclusions

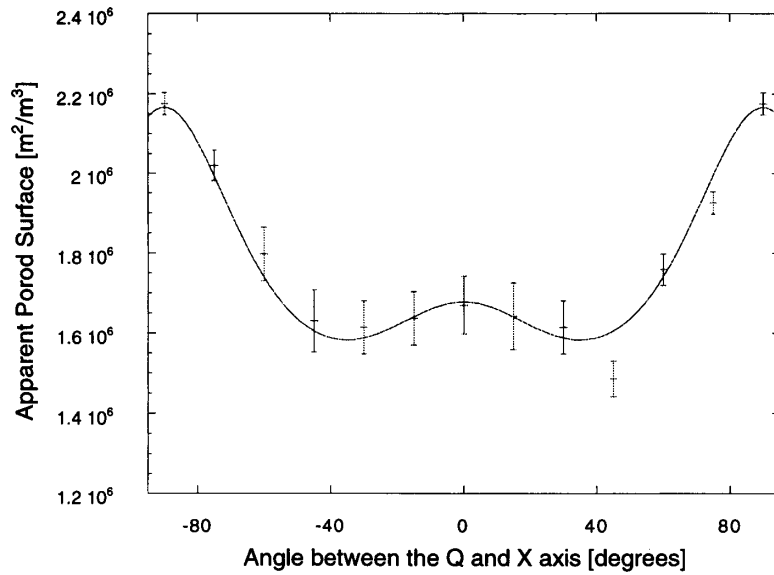
Two distinct systems of voids were observed by means of SANS in plasma-sprayed deposits of gray alumina. One void system is that of the interlamellar pores, where the pores are mostly parallel to the substrate. The other void system is that of the intralamellar cracks, where the cracks are mostly perpendicular to the substrate (for the 90° spray-angle case). More than 80% of the total surface area can be attributed to the cracks in these deposits.

The two void systems exhibit different dependences on the spray angle. The orientation of the interlamellar pores does not change with the spray direction. Intralamellar cracks, however, tilt toward the spray direction. A plausible explanation for this effect would be that it results from changes in the texture,³⁶ or preferred crystallographic orientation, of the grains within the splats themselves as the spray angle changes. The underlying cause of the texturing may result from the change in the splat-cooling direction during deposition, which is related to the splat-impact direction. Alternatively, the cracking may result from the change in the heat-flow direction upon cooling.

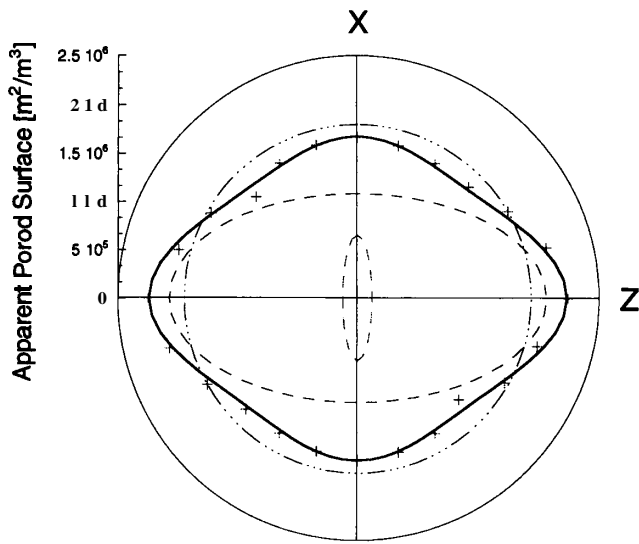
The amount of porosity increases slowly with decreasing spray angle, from 90° down to 50°, until 30° when a large increase in the porosity was found. In contrast, the MIP results indicate an increase in the mean pore size, even for the smallest decrease in the spray angle. This suggests that the character of the voids changes, even while the total volume and the total surface area of the voids do not change significantly.

The SANS results indicate that one of the void systems is preferentially oriented parallel to the splats (substrate surface) and the other is preferentially oriented normal to the splats (parallel to the spray direction) for a 90° spray angle. The parameters observed for the interlamellar pores are consistent with McPherson's model of 0.1- μm -thick, disk-shaped intersplat voids,³⁷ which is in turn supported by thermal conductivity measurements. Concerning the voids parallel to the spray direction, these are attributed to microcracks which form on cooling during and immediately following the spray process. The prevailing orientation of the cracks depends on the spray direction, and the SANS Porod scattering studies indicate that the preferred orientation is tilted away from the direction orthogonal to the substrate and towards the spray direction.

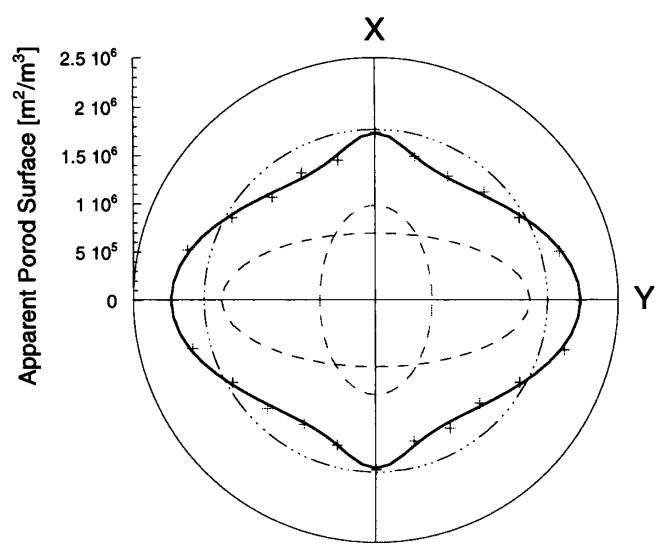
A model of the distribution of cracks and pores in a plasma-sprayed deposit illustrates the influence that such voids can have on the in-service behavior of the deposit. For example, it is widely recognized that cracks perpendicular to the substrate can be converted into fatal delamination cracks on thermal cycling of a ceramic coating on a metallic substrate.^{38,39} Preliminary results of the authors show that there may, however, be a more complex relationship and that, under some conditions,



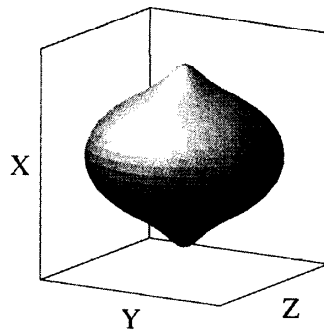
(A)



(B)



(C)



(D)

Fig. 7. Apparent Porod surface area distribution for different orientations of Q. The sample was sprayed at a 90° spray angle. The data are given (A) as a Cartesian plot, where the X axis represents the angle between Q and the X axis. The sample was viewed along the Y axis (i.e., the neutron beam was parallel to the Y axis). In (B) and (C), the data are given in polar coordinates where the distance from the center represents the apparent surface area (converted from the measured Porod constant using Eq. (3)) measured in a given Q direction. Graph (B) represents the sample viewed along the Y axis, while graph (C) represents the sample viewed along the Z axis. Angles are measured between Q and the X axis. The dashed lines show the two surface-area systems resolved. The solid line shows the sum of these two apparent surface-area systems (fitted on the experimental points) and the dash-dotted line represents the true total void surface area obtained by averaging measured values over 4π steradian. Finally, (D) is a three-dimensional illustration of the anisotropy of the apparent surface area distribution from (B) and (C). The linear scale on each axis is -2.5×10^6 to $2.5 \times 10^6 m^2/m^3$, and is omitted for clarity.

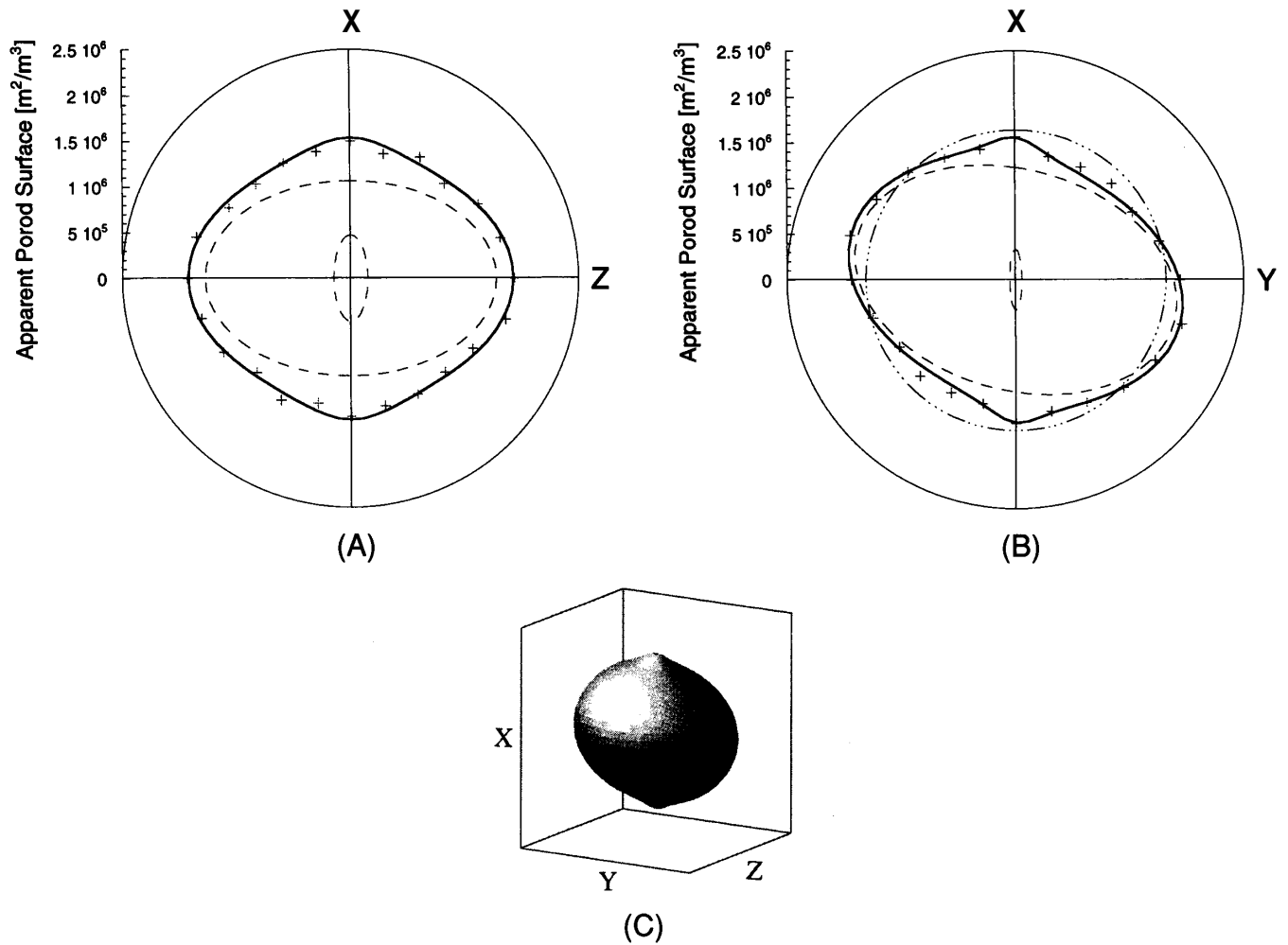


Fig. 8. Apparent Porod surface-area distribution for samples sprayed at a spray angle of 70° . Plots (A) and (B) are in polar coordinates, as above in Figs. 7(B) and (C). The equivalent three-dimensional illustration is given in 8(C).

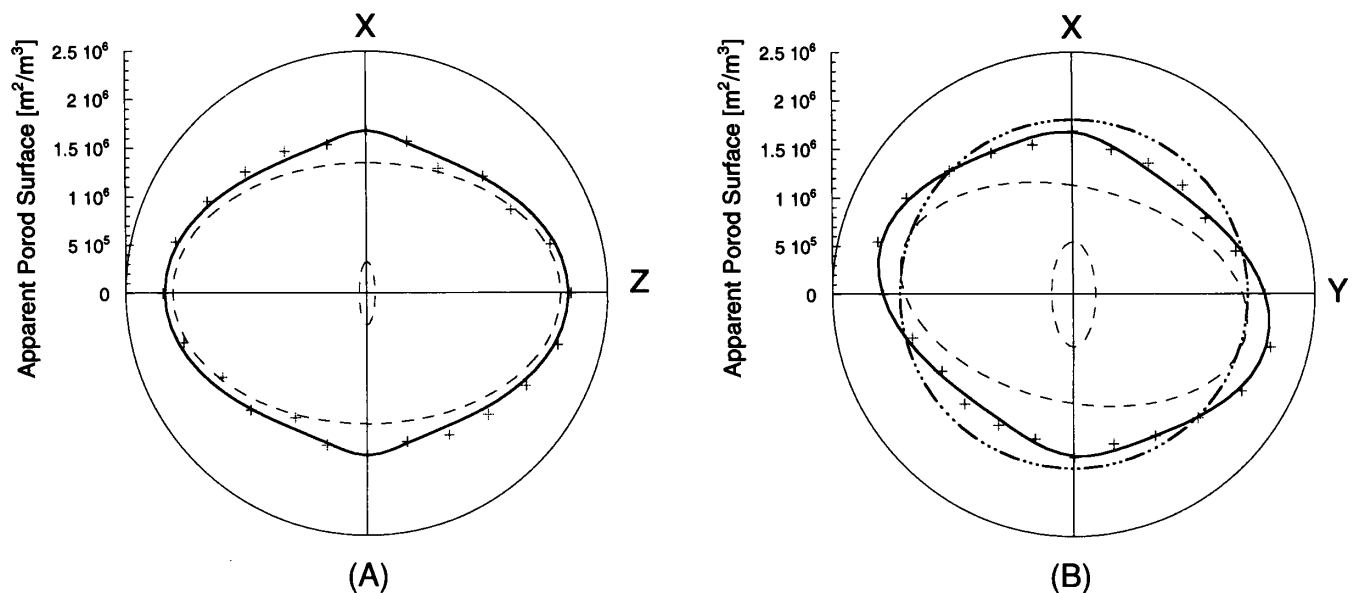


Fig. 9. Apparent Porod surface-area distribution for samples sprayed at a spray angle of 50° . Plots (A) and (B) are in polar coordinates, as in Figs. 7(B) and (C).

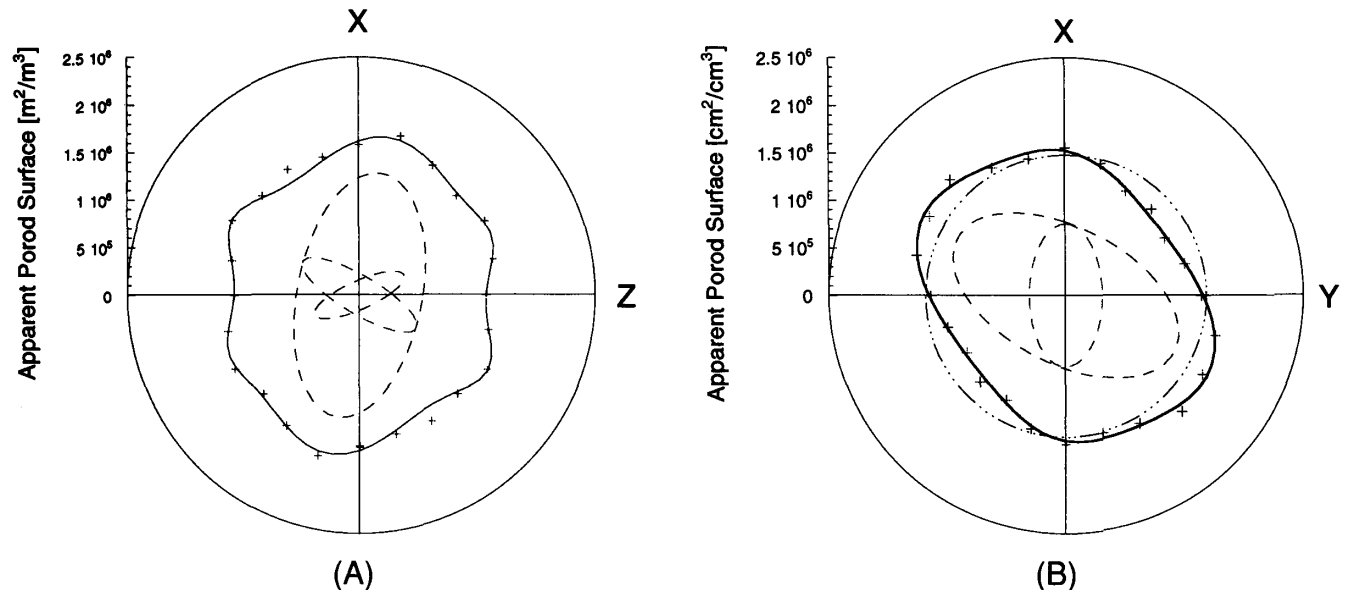


Fig. 10. Apparent Porod surface-area distribution for samples sprayed at a spray angle of 30° . Plots (A) and (B) are in polar coordinates, as above in Figs. 7(B) and (C).

cracks may play a beneficial role in improving the mechanical properties of the deposits. There is also evidence that interlamellar voids parallel to the substrate can act to blunt or stop the propagation of flaws and retard their development into delamination events. It would thus appear that the distribution of porosity in a coating (i.e., the ratio of the numbers of cracks to the number of interlamellar pores) will significantly affect both the thermal conductivity and the probability of coating failure. This concept could be particularly important for plasma-sprayed, high-temperature sections of gas turbine engines in which complex-shaped airfoils are employed in the high-pressure region of the turbine.

Further, on the observed spray angle effects, it has been noted here that the microcracks, as depicted by SANS, appear to tilt toward the spray angle, whereas the thin interlamellar pores remain unchanged with spray angle. If, as is generally considered,^{38,39} the microcrack distribution influences coating survivability, then spray angle will play a prominent role in coating integrity. Therefore, on spraying the airfoils mentioned above, the crack orientation and crack morphology will change as the flame traverses curved regions of the target. Clearly, this phenomenon needs detailed examination, and should be included in future research agendas.

References

- ¹V. V. Kudinov, P. Yu. Pekshev, and V. A. Safiullin, "Forming of the Structure of Plasma-Sprayed Materials"; pp. 381–418 in *High-Temperature Dust Laden Jets in Plasma Technology*, Proceedings of the International Workshop (Novosibirsk, USSR, September 1988). Edited by O. P. Solonenko and A. I. Fedorcenko. VSP BV, Zeist, The Netherlands, 1990.
- ²M. R. Roode and B. Beardsley, "Porosity Determination of Thermal Barrier Coatings"; presentation at the Gas Turbine and Aeroengine Congress (Amsterdam, The Netherlands, 1988).
- ³H. Herman, "Plasma-Sprayed Coatings," *Sci. Am.*, 259 [3] 112–17 (1988).
- ⁴R. McPherson, "The Relationship between the Mechanism of Formation, Microstructure and Properties of Plasma-Sprayed Coatings," *Thin Solid Films*, **83**, 297–310 (1981).
- ⁵R. McPherson and B. V. Shafer, "Interlamellar Contact within Plasma-Sprayed Coatings," *Thin Solid Films*, 97, 201–204 (1982).
- ⁶Y. Arata, A. Ohmori, and Ch.-J. Li, "Study on the Structure of Plasma Sprayed Coating by Using Copper Electroplating"; pp. 205–10 in Proceedings of the International Symposium on Advanced Thermal Spraying Technology and Allied Coatings (Osaka, Japan, May 1988). High Temperature Society of Japan, Osaka, Japan, 1988.
- ⁷L. A. Fisher, "Variables Influencing the Characteristics of Plasma-Sprayed Coatings," *Int. Metall. Rev.*, **17**, 117–29 (1972).
- ⁸H.-D. Steffens and U. Fisher, "Correlation Between Microstructure and Physical Properties of Plasma Sprayed Zirconia"; pp. 167–73 in *Thermal Spray Technology, New Ideas and Processes*, Proceedings of the National Thermal Spray Conference (Cincinnati, OH, October 1988). Edited by D. L. Houck. ASM International, Materials Park, OH, 1988.
- ⁹R. C. Tucker, Jr., and M. O. Price, "The Effect of Angle Deposition on the Properties of Selected Detonation Gun Coatings"; pp. 61–71 in Proceedings of International Symposium on Advanced Thermal Spraying Technology and Allied Coatings (Osaka, Japan, May 1988). High Temperature Society of Japan, Osaka, Japan, 1988.
- ¹⁰A. Hasui, S. Kitahara, and T. Fukushima, "On Relation between Properties of Coating and Spraying Angle in Plasma Jet Spraying," *Trans. Natl. Res. Inst. Met. (Jpn.)*, **12** [1] 9–20 (1970).
- ¹¹K. T. Scott and R. Kingswell, "Thermal Spraying"; pp. 217–43 in *Advanced Surface Coatings: A Handbook of Surface Engineering*. Blackie & Son Limited, Bishopbriggs, Glasgow, U.K., 1991.
- ¹²S.-H. Leigh and C. C. Bemdt, "Evaluation of Off-Angle Plasma Spray," submitted to *J. Surf. Coating Technol.*
- ¹³G. Montavon, C. Coddet, S. Sampath, H. Herman, and C. C. Bemdt, "Vacuum Plasma Spray Forming of Astroloy: An Investigation of Processing Parameters"; pp. 469–75 in *1994 Thermal Spray Industrial Applications*, Proceedings of the 7th National Thermal Spray Conference (Boston, MA, June 1994). Edited by C. C. Bemdt and S. Sampath. ASM International, Materials Park, OH, 1994.
- ¹⁴R. Gansert, S. Sampath, C. C. Bemdt, H. Herman, J. Ilavsky, and P. Chraska, "The Processing of Free-Standing Ceramic Deposits by Water-Stabilized Plasma Spraying," unpublished work.
- ¹⁵V. S. Thompson and O. J. Whittemore, Jr., "Structural Changes on Reheating Plasma-Sprayed Alumina," *Am. Ceram. Soc. Bull.*, **47** [7] 637–41 (1968).
- ¹⁶J. Wang, C. B. Ponton, and P. M. Marquis, "A Quantitative X-ray Diffraction Phase Analysis in the Reaction-Sintered Mullite Ceramics," *J. Mater. Sci. Lett.*, **11**, 1301–304 (1992).
- ¹⁷R. Fillit, P. Homerin, J. Schafer, H. Bruyas, and F. Thevenot, "Quantitative X-ray Diffraction Analysis of Zirconia-Toughened Alumina Ceramics," *J. Mater. Sci.*, **22**, 3566–70 (1987).
- ¹⁸B. Freudenberg and A. Mocellin, "Alumina Titanate Formation by Solid State Reaction of Fine Al_2O_3 and TiO_2 Powders," *J. Am. Ceram. Soc.*, **70** [1] 33–38 (1987).
- ¹⁹H. K. Schmid, "Quantitative Analysis of Polymorphic Mixes of Zirconia by X-ray Diffraction," *J. Am. Ceram. Soc.*, **70** [5] 367–76 (1987).
- ²⁰B. L. Davis, "Quantitative Reference Intensity Analysis: Methodology and Means for Verification of Results"; pp. 15–21 in *X-ray and Neutron Structure Analysis in Materials Science*, Proceedings of the International Conference on Advanced Methods in X-ray and Neutron Structure Analysis of Materials (Karlovy Vary, Czechoslovakia, 1987). Edited by J. Hasek. Plenum Press, New York, 1987.
- ²¹J. Ilavsky, "Studies of Plasma Sprayed Alumina"; Ph.D. Dissertation. State University of New York, Stony Brook, NY, 1994.
- ²²S. J. Gregg and K. S. W. Sing, *Adsorption, Surface Area and Porosity*; pp. 173–95. Academic Press, London, U.K., 1982.
- ²³H. H. D. Lee, "Validity of Using Mercury Porosimetry to Characterize the Pore Structure of Ceramic Green Compacts," *J. Am. Ceram. Soc.*, **73** [8] 2309–15 (1990).
- ²⁴Standard Test Method for Measurement of Density of Glass by Buoyancy," ASTM C693-84, American Society for Testing and Materials, Philadelphia, PA, 1985.
- ²⁵S. Krueger, G. G. Long, and R. A. Page, "Characterization of the Densification of Alumina by Multiple Small-Angle Neutron Scattering," *Acta Crystallogr.*, **A47**, 282–90 (1991).
- ²⁶G. G. Long, S. Krueger, R. A. Gerhardt, and R. A. Page, "Small-Angle Neutron Scattering Characterization of Processing/Microstructure Relationships in the Sintering of Crystalline and Glassy Ceramics," *J. Mater. Res.*, **6** [12] 2706–15 (1991).

- ²⁷G. Porod; pp. 17–51 in *Small-Angle X-ray Scattering*. Edited by O. Galtter and O. Kratky. Academic Press, London, U.K., 1982.
- ²⁸G. Kostorz, "Small-Angle Scattering and Its Applications to Materials Science"; pp. 227–90 in *Treatise on Materials Science and Technology*, Vol. 15. Edited by G. Kostorz. Academic Press, New York, 1979.
- ²⁹J. R. Weertman; pp. 147–68 in *Nondestructive Evaluation: Microstructure Characterization and Reliability Strategies*. American Institute of Mining, Metallurgical and Petroleum Engineers, New York, 1981.
- ³⁰F. M. Hamzeh and R. H. Bragg, "Small-Angle Scattering of X-rays from Groups of Nonrandomly Oriented Ellipsoids of Revolution of Low Concentration," *J. Appl. Phys.*, **45** [7] 3189–95 (1974).
- ³¹J. Kärthikeyan; personal communication, 1995.
- ³²J. Ilavsky, H. Herman, C. C. Berndt, A. N. Goland, G. G. Long, S. Krueger, and A. J. Allen, "Porosity in Plasma Sprayed Alumina Coatings"; pp. 709–14 in *1994 Thermal Spray Industrial Applications*, Proceedings of the 1994 National Thermal Spray Conference (Boston, MA, June 1994). Edited by C. C. Berndt and S. Sarnpath. ASM International, Materials Park, OH, 1994.
- ³³A. J. Allen and N. F. Berk, "Analysis of Small-Angle Scattering Data Dominated by Multiple Scattering for Systems Containing Eccentrically Shaped Particles or Pores," *J. Appl. Crystallogr.*, **27**, 878–91 (1994).
- ³⁴J. Ilavsky, A. J. Allen, G. G. Long, S. Krueger, H. Herman, C. C. Berndt, and A. N. Goland, "Anisotropy of the Surfaces of Pores in Plasma Sprayed Alumina Deposits"; pp. 483–88 in *Thermal Spraying—Current Status and Future Trends*, Proceedings of the 14th International Thermal Spray Conference (Kobe, Japan, May 1995). Edited by A. Ohmori. High Temperature Society of Japan, Osaka, Japan, 1995.
- ³⁵P. Yu. Pekshev and V. A. Safiullin, "Porosity of Plasma Sprayed Alumina"; pp. 437–62 in *High-Temperature Dust Laden Jets in Plasma Technology*, Proceedings of the International Workshop (Novosibirsk, USSR, September 1988). Edited by O. P. Solonenko and A. I. Fedorcenko. VSP BV, Zeist, The Netherlands, 1990.
- ³⁶S. Safai and H. Herman, "Plasma Sprayed Coatings: Their Ultramicrostructure"; paper 5 in *Advances in Surface Coating Technology*, Proceedings of the International Conference (London, February 1978). Welding Institute, London, U.K., 1978.
- ³⁷R. McPherson, "A Review of Microstructure and Properties of Plasma Sprayed Ceramic Coatings," *Surf. Coating Technol.*, **39/40**, 173–81 (1989).
- ³⁸K. Kokini and Y. R. Takeuchi, "Initiation of Surface Cracks in Multilayer Ceramic Thermal Barrier Coatings under Thermal Loads," *Mater. Sci. Eng.*, **A189**, 301–309 (1994).
- ³⁹Y. R. Takeuchi and K. Kokini, "Thermal Fracture of Multilayer Ceramic Thermal Barrier Coatings," *J. Eng. Gas Turbines Power*, **1167**, 266–71 (1994). □